frontiers | Frontiers in Energy Research

TYPE Original Research
PUBLISHED 19 May 2025
DOI 10.3389/fenrg.2025.1602269

OPEN ACCESS

EDITED BY
Wenping Zhang,
Tianjin University, China

REVIEWED BY
Yinxiao Zhu,
Zhejiang University, China
Baiyi Liu,
Shanghai Jiao Tong University, China

*CORRESPONDENCE
Jikai Li,
lijikai@xj.cee-group.cn

RECEIVED 29 March 2025
ACCEPTED 28 April 2025
PUBLISHED 19 May 2025

CITATION
Feng Q, Li J, Zhou J, Xu Y, He Q and Gao Y (2025) A coordinated power quality improvement control strategy for AC/DC hybrid distribution networks based on three-phase four-leg flexible interconnection converter.
Front. Energy Res. 13:1602269.
doi: 10.3389/fenrg.2025.1602269

A coordinated power quality improvement control strategy for AC/DC hybrid distribution networks based on three-phase four-leg flexible interconnection converter

Qihui Feng[1], Jikai Li[2]*, Junchao Zhou[1], Yutao Xu[1], QingLian He[2] and Yuan Gao[1]

[1]Electric Power Research Institute of Guizhou Power Grid Co. Ltd., Guiyang, China, [2]XJ Electric Co. Ltd., Xuchang, China

In this paper, A coordinated power quality improvement control strategy for three-phase four-Leg flexible interconnection converter (3P4L-FIC) based AC/DC hybrid distribution networks is proposed, which can address three-phase unbalance issues in AC area and double frequency ripple issue in DC area simultaneously without extra components. Firstly, for the problems of three-phase load unbalance in the AC station area, the split-phase power decoupling control based power quality optimization is delivered for 3P4L-FIC based hybrid distribution networks. Secondly, the doubling frequency pulsation mechanism of DC bus voltage during three-phase unbalanced compensation conditions is analyzed in detail, and a DC voltage doubling frequency ripple migration scheme based on hybrid proportional-integral and resonant controller (PI-R) is proposed. Finally, the 3P4L-FIC based low-voltage multi-distribution area simulation model constructed by Matlab/Simulink is verified, and the results show that the three-phase imbalance of the low-voltage AC line is completely compensated, and the double-frequency ripple of the DC bus voltage is greatly reduced, which realizes the synergistic enhancement of the power quality of the AC-DC distribution area.

KEYWORDS

power quality improvement, three-phase four-bridge-arm converter, unbalance compensation, double-frequency ripple, flexible interconnection

1 Introduction

With the advancement of the "dual-carbon" goals, distributed renewable energy and electrified loads are rapidly integrated into low-voltage distribution networks, leading to prominent issues such as three-phase imbalance and voltage violations (Xu et al., 2022; Mocci et al., 2025; Tang et al., 2023). The flexible interconnection system for distribution areas employs power electronic conversion devices to establish flexible DC channels between and within distribution areas (Shi et al., 2023; Liu et al., 2023; Sheng et al., 2024). This system enables power quality management in AC distribution areas, dynamic capacity expansion of distribution areas, and efficient/reliable accommodation of large-scale high-penetration distributed generation and high-proportion electrified terminal loads (Xiao et al., 2024; Si et al., 2024; Cai et al., 2023; Zheng et al., 2024; Wang et al., 2008).

Compared with conventional three-leg four-wire flexible interconnection converters, three-phase four-leg (3P4L) converters offer advantages including higher DC voltage utilization, reduced requirements for DC-side input capacitance, and effective control of zero-sequence components. These merits have gradually made them a research hotspot for flexible interconnection converters in distribution areas. Shao and Ma (2008), Lu et al. (2020) implemented individual phase voltage control based on established mathematical models of three-phase four-leg inverters, but their control loops lack complete decoupling, resulting in suboptimal performance. Sun et al. (2020), Zhang et al. (2017), Tan et al. (2019) proposed sequence decomposition strategies combined with feedforward methods to address asymmetric output voltage issues through sequence-decoupled control, though grid harmonics were not considered. Yan et al. (2018), Nguyen and Choi (2018) utilized repetitive controllers to suppress harmonic components and improve grid current quality in three-phase four-leg grid-connected inverters, but their control structures and parameter tuning remain relatively complex.

However, the previous studies effectively address unbalanced loads and harmonic suppression on the AC side but fail to consider that double-frequency instantaneous power fluctuations caused by negative-sequence and zero-sequence components under three-phase AC imbalance conditions propagate to the DC side, inducing double-frequency disturbances. Current solutions for double-frequency power decoupling mainly include passive and active power decoupling methods. Passive power decoupling employs large parallel capacitors (Zeng et al., 2018) or LC resonant circuits (Wang et al., 2024) to absorb double frequency power but suffers from high implementation costs and limited effectiveness. Active power decoupling utilizes switching devices to exchange power with decoupling capacitors for pulsating power compensation (Tao et al., 2023; Huang et al., 2023; Zhang et al., 2023; Luo et al., 2023; Fan et al., 2023; Xu et al., 2020). While enhanced switching configurations improve secondary ripple suppression, they simultaneously escalate system power losses. Tan et al. (2025) proposes a control strategy for three-phase four-leg PWM rectifier under unbalanced grid voltage conditions, which aims at achieving not only no second harmonic in dc output voltage, but also unity power factor operation for each phase. Zhou and Lu (2025), Bhowmick et al. (2025) used an active power decoupling (APD) or boost converter circuit to suppression the double-frequency disturbances in DC bus, while the additional APD circuit will increase the system cost.

To address these limitations, this paper proposes a coordinated AC-DC distribution area power quality optimization strategy based on split-phase power decoupling and resonant control, comprehensively considering three-phase imbalance, voltage violations in AC distribution areas, and double-frequency ripple issues in DC distribution areas. The strategy is implemented within the three-phase four-leg flexible interconnected converter (3P4L-FIC) based distribution area architecture shown in Figure 1. Specifically, a power decoupling control strategy based on positive-negative-zero sequence separation is introduced at the inverter side (VSC2) to address the three-phase load unbalance issues.

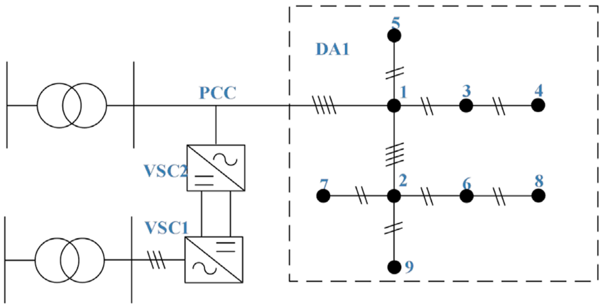

FIGURE 1
Diagram of 3P4L-FIC based AC/DC hybrid distribution networks.

Simultaneously, a resonant-based double-frequency current suppression strategy is implemented at the flexible interconnection rectifier (VSC1) side to mitigate double-frequency voltage ripples in DC distribution areas. The proposed strategy can address three-phase unbalance issues in AC area and double frequency ripple issue in DC area simultaneously without extra components.

The rest of this study is structured thus. Section 2 presents the mathematical model of 3P4L Converters. Section 3 presents a mechanism of double-frequency DC voltage ripples under unbalanced operating conditions. Section 4 proposes a coordinated power quality improvement strategy for AC-DC distribution areas. Section 5 gives simulation validation and analysis, and Section 6 summarizes the key conclusions drawn from our study.

2 Mathematical model of three-phase four-leg converters

Conventional three-phase three-leg converters exhibit interphase coupling in output power, thereby lacking the capability for independent three-phase power regulation. In contrast, the 3P4L-FIC introduces a zero-sequence leg to the traditional three-leg topology (as illustrated in Figure 2), enabling each port to generate independent voltages, which structural enhancement facilitates decoupled control of unbalanced three-phase power.

Using the current through the filter inductor L_f of the three-phase four-leg inverter $\langle i_f \rangle_{Ts}$, the voltage across the capacitor $\langle u_f \rangle_{Ts}$, and the current $\langle i_g \rangle_{Ts}$ through the load-side filter inductor L_g as state variables, and defining the input voltage $\langle u_{dc} \rangle_{Ts}$, input current $\langle i_p \rangle_{Ts}$, and output voltage $\langle u_{kn} \rangle_{Ts}$ as output variables ($k = a$, b, c), the state-space equations can be formulated as follows

$$\frac{d}{dt}\begin{bmatrix} \langle i_{af} \rangle_{Ts} \\ \langle i_{bf} \rangle_{Ts} \\ \langle i_{cf} \rangle_{Ts} \end{bmatrix} + \frac{R}{L_f}\begin{bmatrix} \langle i_{af} \rangle_{Ts} \\ \langle i_{bf} \rangle_{Ts} \\ \langle i_{cf} \rangle_{Ts} \end{bmatrix} = \frac{1}{L_f}\begin{bmatrix} d_{af}\langle V_{dc} \rangle_{Ts} \\ d_{bf}\langle V_{dc} \rangle_{Ts} \\ d_{cf}\langle V_{dc} \rangle_{Ts} \end{bmatrix} - \frac{1}{L_f}\begin{bmatrix} \langle u_{af} \rangle_{Ts} \\ \langle u_{bf} \rangle_{Ts} \\ \langle u_{cf} \rangle_{Ts} \end{bmatrix} + \frac{L_n}{L_f}\frac{d\langle i_n \rangle_{Ts}}{dt} \tag{1}$$

$$\frac{d}{dt}\begin{bmatrix} \langle u_{af} \rangle_{Ts} \\ \langle u_{bf} \rangle_{Ts} \\ \langle u_{cf} \rangle_{Ts} \end{bmatrix} = \frac{1}{C_f}\begin{bmatrix} \langle i_{af} \rangle_{Ts} \\ \langle i_{bf} \rangle_{Ts} \\ \langle i_{cf} \rangle_{Ts} \end{bmatrix} - \frac{1}{C_f}\begin{bmatrix} \langle i_{ag} \rangle_{Ts} \\ \langle i_{bg} \rangle_{Ts} \\ \langle i_{cg} \rangle_{Ts} \end{bmatrix} \tag{2}$$

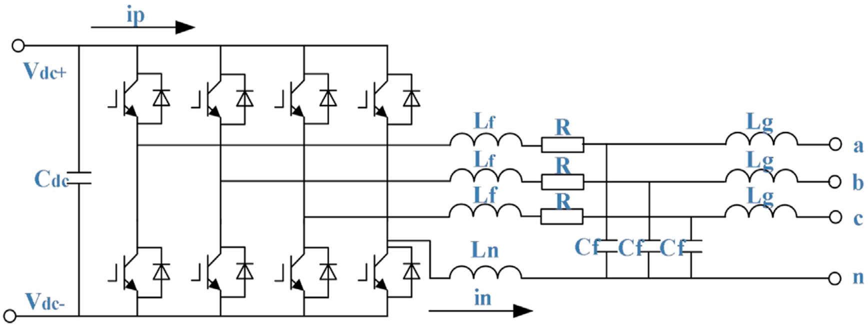

FIGURE 2
Topology architecture of three-phase four-leg converter.

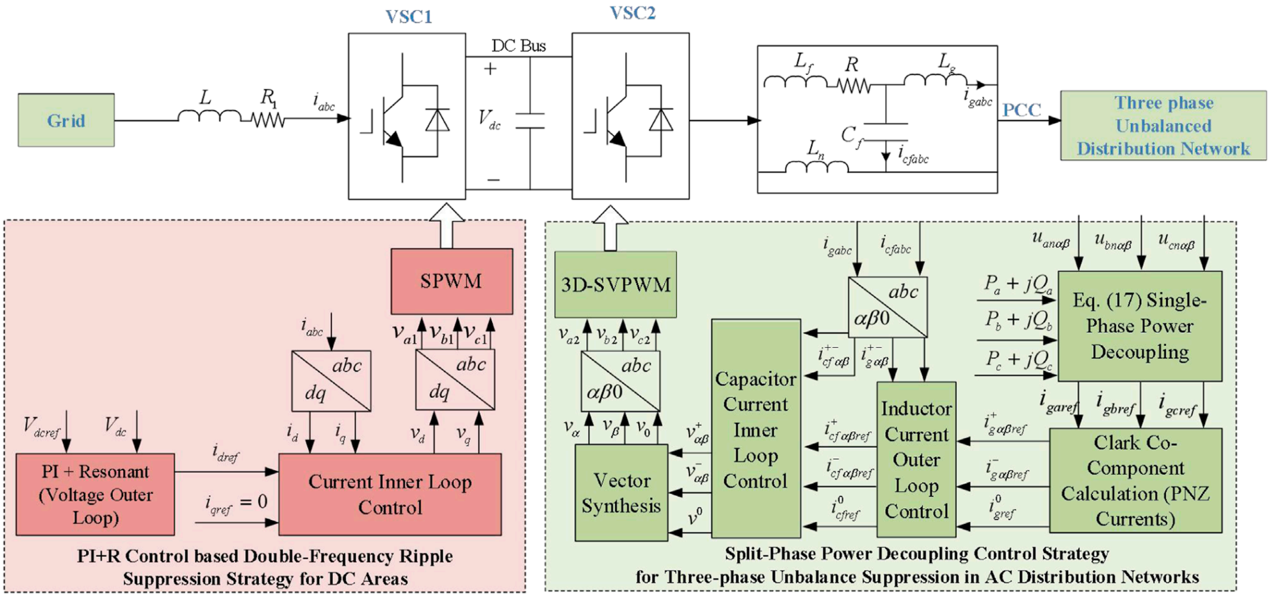

FIGURE 3
Overall diagram of the proposed coordinated power quality improvement strategy for 3P4L-FIC based AC-DC distribution areas.

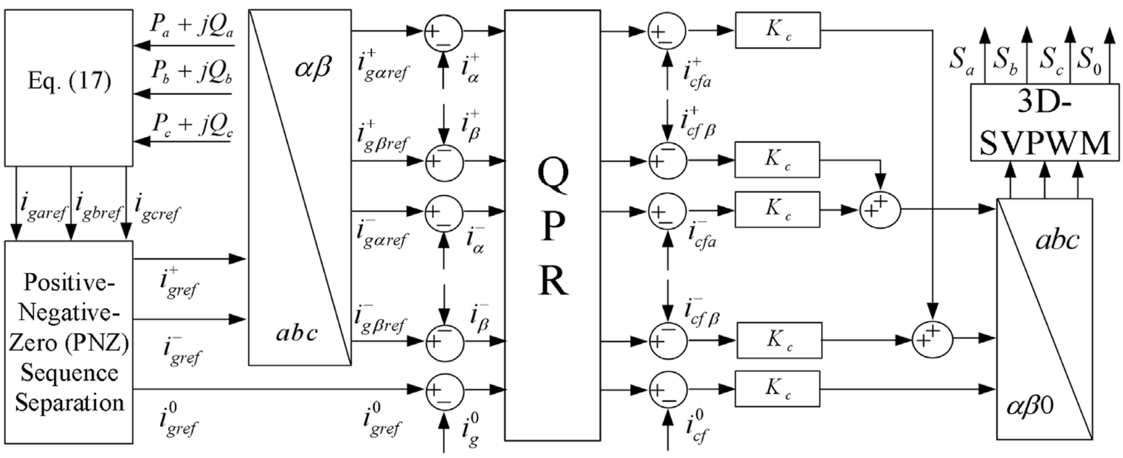

FIGURE 4
The overall control block diagram of the proposed split-phase power decoupling strategy in VSC2.

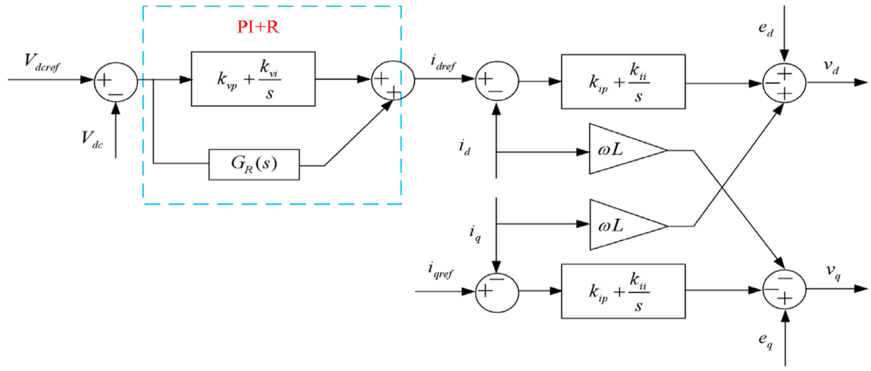

FIGURE 5
The overall control block diagram of PI-R control based double-frequency ripple suppression strategy in VSC1.

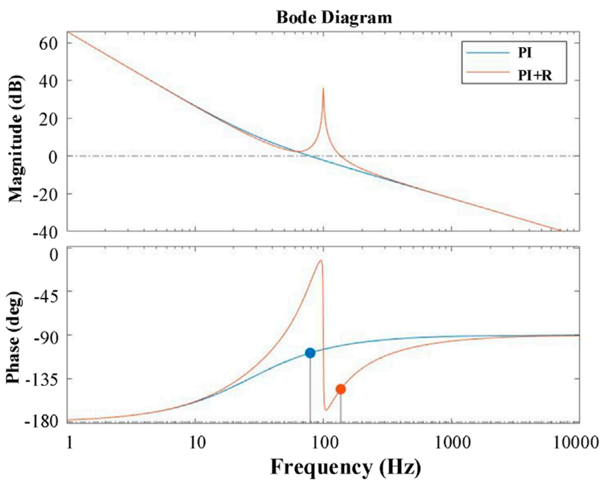

FIGURE 6
Comparison bode diagram between PI and PI-R outer loop.

TABLE 1 System parameters.

Parameters	Value/Unit	Parameters	Value/Unit
L	7e-3/H	R	1e-2/Ω
R_1	1e-2/Ω	C_f	5e-6/F
C_{dc}	3.8e-3/F	L_g	1e-3/H
L_f	5e-3/H	L_n	7e-4/H

TABLE 2 Control parameters.

Parameters	Value	Parameters	Value
K_p	1	K_{rr}	12
ω_{cr}	5	ω_{0r}	314

$$\frac{d}{dt}\begin{bmatrix}\langle i_{ag}\rangle_{Ts}\\ \langle i_{bg}\rangle_{Ts}\\ \langle i_{cg}\rangle_{Ts}\end{bmatrix}=\frac{1}{L_g}\begin{bmatrix}\langle u_{af}\rangle_{Ts}\\ \langle u_{bf}\rangle_{Ts}\\ \langle u_{cf}\rangle_{Ts}\end{bmatrix}-\frac{1}{L_g}\begin{bmatrix}\langle u_{an}\rangle_{Ts}\\ \langle u_{bn}\rangle_{Ts}\\ \langle u_{cn}\rangle_{Ts}\end{bmatrix}\tag{3}$$

Where i_{kf} and i_{kg} represent the currents flowing through inductors L_f and L_g in phase k, respectively. u_{kf} and u_{kn} denote the voltage across capacitor C_f and the converter output voltage in phase k, respectively. d_{kf} $(k = a,b,c)$ is the phase duty cycle, derived by averaging the switching functions of the bridge-arm switches over a switching period and filtering out switching-frequency harmonic components. i_n corresponds to the current flowing through inductor L_n.

From Equations 1–3, it is evident that if the neutral inductor and its equivalent resistance are neglected, the three-phase four-leg inverter system reduces to three independent single-phase full-bridge inverter systems. When the neutral inductor is considered, however, mutual coupling arises between the bridge legs, preventing the system from being treated as three decoupled inverter units. This observation underscores the inherent difficulty in achieving decoupled control of the three-phase four-leg inverter in the three-phase stationary coordinate frame.

Translating the fundamental sinusoidal components from the three-phase stationary coordinate frame into a two-phase stationary coordinate frame, followed by Laplace transformation, yields the system's frequency-domain control model, expressed as

$$s\begin{bmatrix}\langle i_{\alpha f}\rangle_{Ts}\\ \langle i_{\beta f}\rangle_{Ts}\\ \langle i_{0f}\rangle_{Ts}\end{bmatrix}+\frac{R}{L_f}\begin{bmatrix}\langle i_{\alpha f}\rangle_{Ts}\\ \langle i_{\beta f}\rangle_{Ts}\\ \langle i_{0f}\rangle_{Ts}\end{bmatrix}=\frac{1}{L_f}\begin{bmatrix}d_{\alpha f}\langle V_{dc}\rangle_{Ts}\\ d_{\beta f}\langle V_{dc}\rangle_{Ts}\\ d_{0f}\langle V_{dc}\rangle_{Ts}\end{bmatrix}-\frac{1}{L_f}\begin{bmatrix}\langle u_{\alpha f}\rangle_{Ts}\\ \langle u_{\beta f}\rangle_{Ts}\\ \langle u_{0f}\rangle_{Ts}\end{bmatrix}+\frac{3L_n s}{L_f}\langle i_0\rangle_{Ts}\tag{4}$$

$$s\begin{bmatrix}\langle u_{\alpha f}\rangle_{Ts}\\ \langle u_{\beta f}\rangle_{Ts}\\ \langle u_{0f}\rangle_{Ts}\end{bmatrix}=\frac{1}{C_f}\begin{bmatrix}\langle i_{\alpha f}\rangle_{Ts}\\ \langle i_{\beta f}\rangle_{Ts}\\ \langle i_{0f}\rangle_{Ts}\end{bmatrix}-\frac{1}{C_f}\begin{bmatrix}\langle i_{ag}\rangle_{Ts}\\ \langle i_{bg}\rangle_{Ts}\\ \langle i_{cg}\rangle_{Ts}\end{bmatrix}\tag{5}$$

$$s\begin{bmatrix}\langle i_{\alpha g}\rangle_{Ts}\\ \langle i_{\beta g}\rangle_{Ts}\\ \langle i_{0g}\rangle_{Ts}\end{bmatrix}=\frac{1}{L_g}\begin{bmatrix}\langle u_{\alpha f}\rangle_{Ts}\\ \langle u_{\beta f}\rangle_{Ts}\\ \langle u_{0f}\rangle_{Ts}\end{bmatrix}-\frac{1}{L_g}\begin{bmatrix}\langle u_{\alpha n}\rangle_{Ts}\\ \langle u_{\beta n}\rangle_{Ts}\\ \langle u_{0n}\rangle_{Ts}\end{bmatrix}\tag{6}$$

TABLE 3 Three phase load and photovoltaic access data for distributor area I (Scenario 1).

Nodes	Load/kW			PV/kW		
	Phase A	Phase B	Phase C	Phase A	Phase B	Phase C
1	1.22	1.22	1.22	7.3	3.65	0
2	1.22	1.22	1.22	0	3.65	1.825
3	0	1.22	0	0	1.825	0
4	0	1.22	0	0	1.825	0
5	4.88	0	0	7.3	0	0
6	0	0	1.22	0	0	1.825
7	1.22	0	0	1.825	0	0
8	0	0	1.22	0	0	0
9	0	1.22	0	0	1.825	0

TABLE 4 Three phase load and photovoltaic access data for distribution area I (Scenario 2).

Nodes	Load (kW)			PV(kW)		
	Phase A	Phase B	Phase C	Phase A	Phase B	Phase C
1	3.319	3.319	3.319	0.409	0.103	0
2	3.319	3.319	3.319	0	0.103	0.103
3	0	3.319	0	0	0.103	0
4	0	3.319	0	0	0.103	0
5	13.28	0	0	0.409	0	0
6	0	0	3.319	0	0	0.103
7	3.319	0	0	0.103	0	0
8	0	0	3.319	0	0	0
9	0	3.319	0	0	0.103	0

It can be seem from the Equations 4–6 that under small-signal perturbations around the quiescent operating point, since the DC voltage V_{dc} is regulated under constant-voltage control by Distribution Area II (DA II), the perturbation in V_{dc} is neglected during small-signal analysis of the inverter. Consequently, by separating the DC components and eliminating second-order differential terms at the quiescent operating point, the small-signal model in the rotating coordinate frame is derived as

$$\left(s+\frac{R}{L_f}\right)\begin{bmatrix}\hat{i}_{\alpha f}\\ \hat{i}_{\beta f}\\ \hat{i}_{0f}\end{bmatrix}=\frac{1}{L_f}\begin{bmatrix}d_{\alpha f}V_{dc}\\ d_{\beta f}V_{dc}\\ d_{0f}V_{dc}\end{bmatrix}-\frac{1}{L_f}\begin{bmatrix}\hat{u}_{\alpha f}\\ \hat{u}_{\beta f}\\ \hat{u}_{0f}\end{bmatrix}+\frac{3L_n s}{L_f}\hat{i}_0 \tag{7}$$

$$s\begin{bmatrix}\hat{u}_{\alpha f}\\ \hat{u}_{\beta f}\\ \hat{u}_{0f}\end{bmatrix}=\frac{1}{C_f}\begin{bmatrix}\hat{i}_{\alpha f}\\ \hat{i}_{\beta f}\\ \hat{i}_{0f}\end{bmatrix}-\frac{1}{C_f}\begin{bmatrix}\hat{i}_{\alpha g}\\ \hat{i}_{\beta g}\\ \hat{i}_{0g}\end{bmatrix} \tag{8}$$

$$s\begin{bmatrix}\hat{i}_{\alpha f}\\ \hat{i}_{\beta f}\\ \hat{i}_{0f}\end{bmatrix}=\frac{1}{L_g}\begin{bmatrix}\hat{u}_{\alpha f}\\ \hat{u}_{\beta f}\\ \hat{u}_{0f}\end{bmatrix}-\frac{1}{L_g}\begin{bmatrix}\hat{u}_{\alpha n}\\ \hat{u}_{\beta n}\\ \hat{u}_{0n}\end{bmatrix} \tag{9}$$

From Equations 7–9, it can be observed that the mathematical model of the three-phase four-leg converter is mutually decoupled in the α axis, β axis and *0*-axis, which facilitates controller design and simplifies the implementation of three-phase decoupled control. Furthermore, the mathematical model of the $\alpha\beta$-axis is identical to

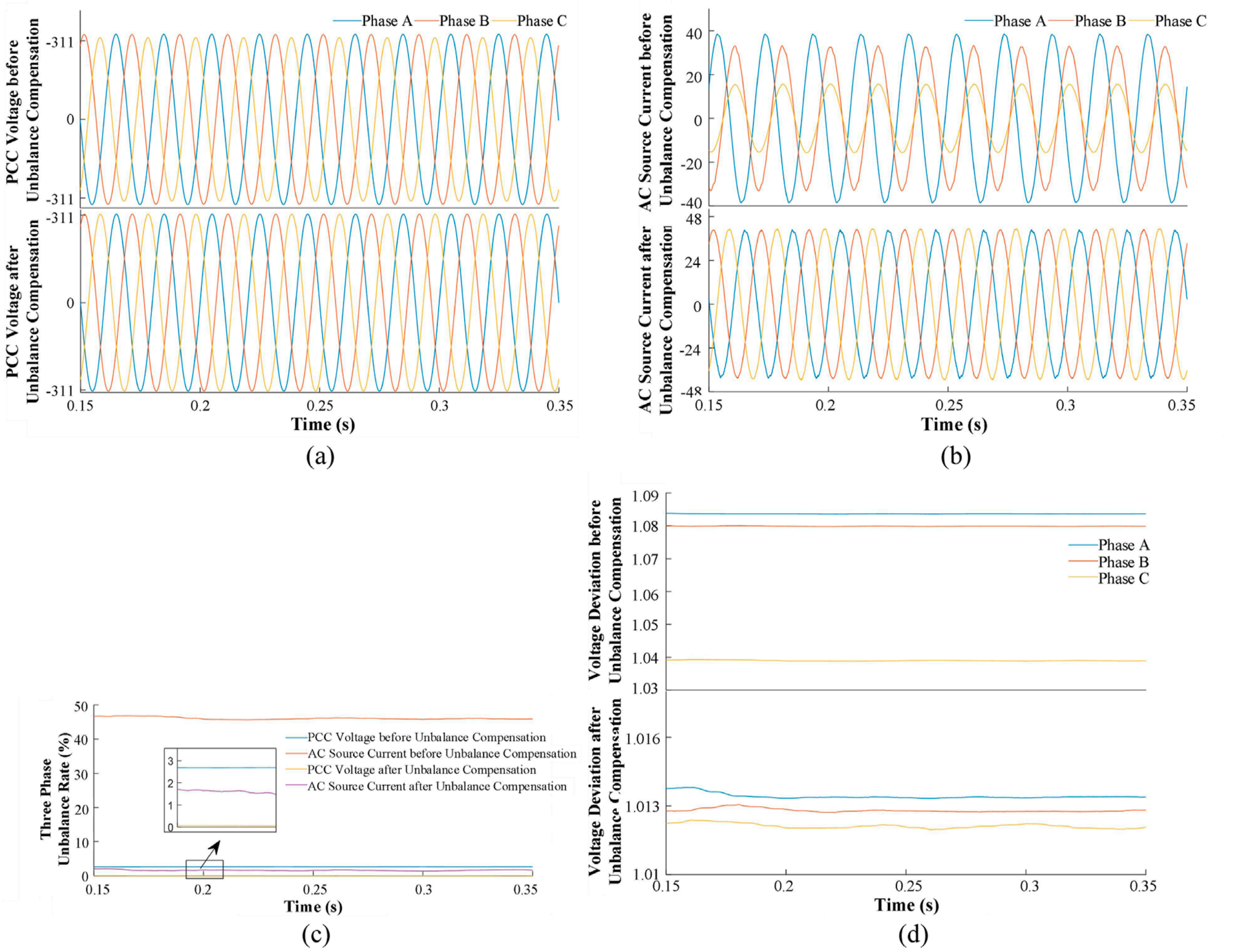

FIGURE 7
Comparison waveform under scenario 1 before and after the unbalance compensation. **(a)** PCC Voltage Waveform. **(b)** Grid AC Source Output Current Waveform. **(c)** Three-Phase Unbalance Rate. **(d)** Voltage Deviation.

that of a conventional three-phase three-leg converter, while the *0*-axis mathematical model incorporates coupling with three times the zero-sequence inductance L_n.

3 Mechanism of DC double frequency voltage ripple under unbalanced operating conditions

The three-phase four-leg inverter is directly connected to the low-voltage distribution network via an *LCL* filter. In the three-phase four-wire system, due to the inclusion of zero-sequence voltage and current components, the system's instantaneous real power p, instantaneous imaginary power q, and instantaneous zero-sequence power p_0 are defined (Akagi et al., 2007) as follows (with coordinate transformation applied for constant-power transformation)

$$\begin{bmatrix} p_0 \\ p \\ q \end{bmatrix} = \begin{bmatrix} v_0 & 0 & 0 \\ 0 & v_\alpha & v_\beta \\ 0 & v_\beta & -v_\alpha \end{bmatrix} \begin{bmatrix} i_0 \\ i_\alpha \\ i_\beta \end{bmatrix} \tag{10}$$

It can be seem from Equation 10 that the zero-sequence instantaneous power in the system is independent of the positive- and negative-sequence instantaneous powers. According to (Dong et al., 2020; Gao et al., 2016), the instantaneous complex power output from the converter's AC side can be expressed as (excluding the zero-sequence component).

$$\begin{cases} p = P_0 + P_{c2}\cos(2\omega t) + P_{s2}\sin(2\omega t) \\ q = Q_0 + Q_{c2}\cos(2\omega t) + Q_{s2}\sin(2\omega t) \end{cases} \tag{11}$$

In Equation 11, P_0 and Q_0 represent the DC components of the instantaneous active and reactive power, respectively. P_{c2} and P_{s2}

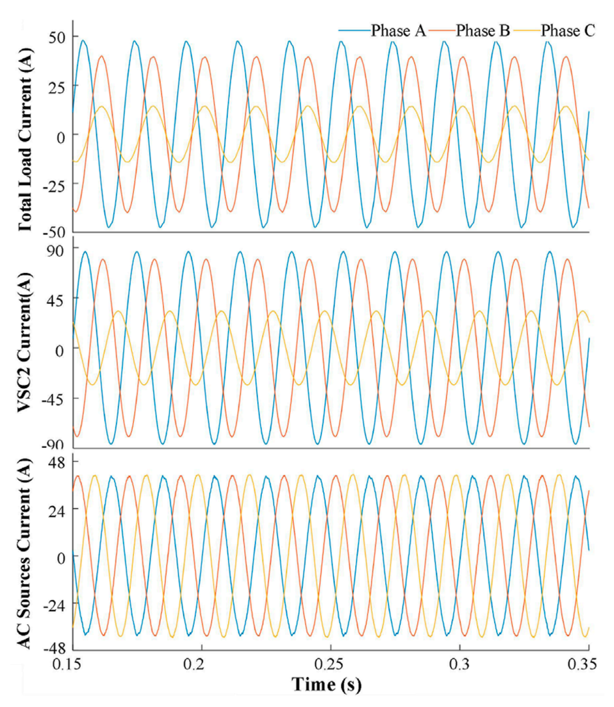

FIGURE 8
The current waveform on the load, AC sources and VSC2 sides under the compensation conditions.

denote the amplitudes of the double-frequency AC components in the instantaneous active power, while Q_{c2} and Q_{s2} correspond to those in the instantaneous reactive power.

The zero-sequence voltage and current components are defined as

$$\begin{cases} u_k^0 = U_0 \cos(\omega t) \\ i_k^0 = I_0 \cos(\omega t + \varphi) \end{cases} (k = a, b, c) \tag{12}$$

In the Equation 12, U_0 and I_0 denote the magnitudes of the zero-sequence voltage and current vectors, respectively. φ represents the phase angle between the zero-sequence voltage and current vectors, and ω is the rotational angular velocity. Therefore, the instantaneous zero-sequence power can be expressed as

$$\begin{cases} p_0 = 3U_0 I_0 \cos\varphi - 3U_0 I_0 \cos(2\omega t + \varphi) \\ q_0 = U_0 I_0 \sin(2\omega t + \varphi) \end{cases} \tag{13}$$

In the equations, p_0 denotes the zero-sequence instantaneous active power, and q_0 represents the zero-sequence instantaneous reactive power. From Equation 13, it is evident that the zero-sequence power itself cannot produce constant power. Therefore, there is no method to eliminate the oscillatory components while retaining only the DC component.

By integrating the above analysis, the total instantaneous power of the three-phase four-wire system is expressed as

$$\begin{cases} p = P_0 + P_{c2}\cos(2\omega t) + P_{s2}\sin(2\omega t) + p_0 \\ q = Q_0 + Q_{c2}\cos(2\omega t) + Q_{s2}\sin(2\omega t) + q_0 \end{cases} \tag{14}$$

From Equation 14, under unbalanced operating conditions, the instantaneous power fluctuations at the second harmonic frequency generated by the negative-sequence and zero-sequence components will penetrate into the DC side, causing second harmonic frequency disturbances in the DC network. This seriously affects the reliability and stability of the system.

4 Coordinated power quality improvement strategy for 3P4L-FIC based AC-DC distribution areas

Figure 3 shows the overall block diagram of the proposed coordinated power quality improved control strategy for 3P4L-FIC distribution areas, which consists of two part. One is the split phase power decoupling control strategy for three phase unbalance compensation of the AC distribution network, which is based on the positive, negative, and zero sequence separation control on the inverter side (VSC2) of the 3P4L-FIC. The other one is hybrid proportional-integral and resonant controller (PI-R) based double-frequency voltage ripple suppression strategy for DC-bus, which is implemented on the rectifier side (VSC1) of the 3P4L-FIC. The proposed coordinated strategy can address three-phase unbalance issues in AC area and double frequency ripple issue in DC area simultaneously without extra components.

4.1 Split-phase power decoupling control based three-phase unbalance compensation strategy for AC distribution areas

Based on the mathematical model of the 3P4L-FIC established in Section 2 under the $\alpha\beta 0$ coordinate frame, and combined with the single-phase power decoupling calculation in Equation 17, the reference command current for split-phase power decoupling is derived. This current is then transformed into positive-, negative-, and zero-sequence reference command currents via Clark transformation, thereby achieving the split-phase power decoupling control strategy. The overall control block diagram of the split-phase power decoupling for *VSC2* is shown in Figure 4.

In the diagram, K_r is the proportional coefficient, and QPR denotes the Quasi-Proportional Resonant (QPR) controller, whose transfer function is expressed as:

$$G_{qpr}(s) = k_{pr} + \frac{2k_{rr}\omega_{cr}s}{s^2 + 2\omega_{cr}s + \omega_{0r}^2} \tag{15}$$

In Equation 15, k_{pr} is the proportional coefficient, k_{rr} is the gain coefficient, ω_{cr} is the bandwidth coefficient, ω_0 is the resonant frequency.

Based on the generalized instantaneous reactive power theory for single-phase systems (Akagi et al., 2007), the $\alpha\beta$ two-phase signals are constructed to obtain the single-phase instantaneous active power and reactive power.

$$\begin{bmatrix} p \\ q \end{bmatrix} = \frac{1}{2}\begin{bmatrix} u_\alpha & u_\beta \\ u_\beta & -u_\alpha \end{bmatrix}\begin{bmatrix} i_\alpha \\ i_\beta \end{bmatrix} \tag{16}$$

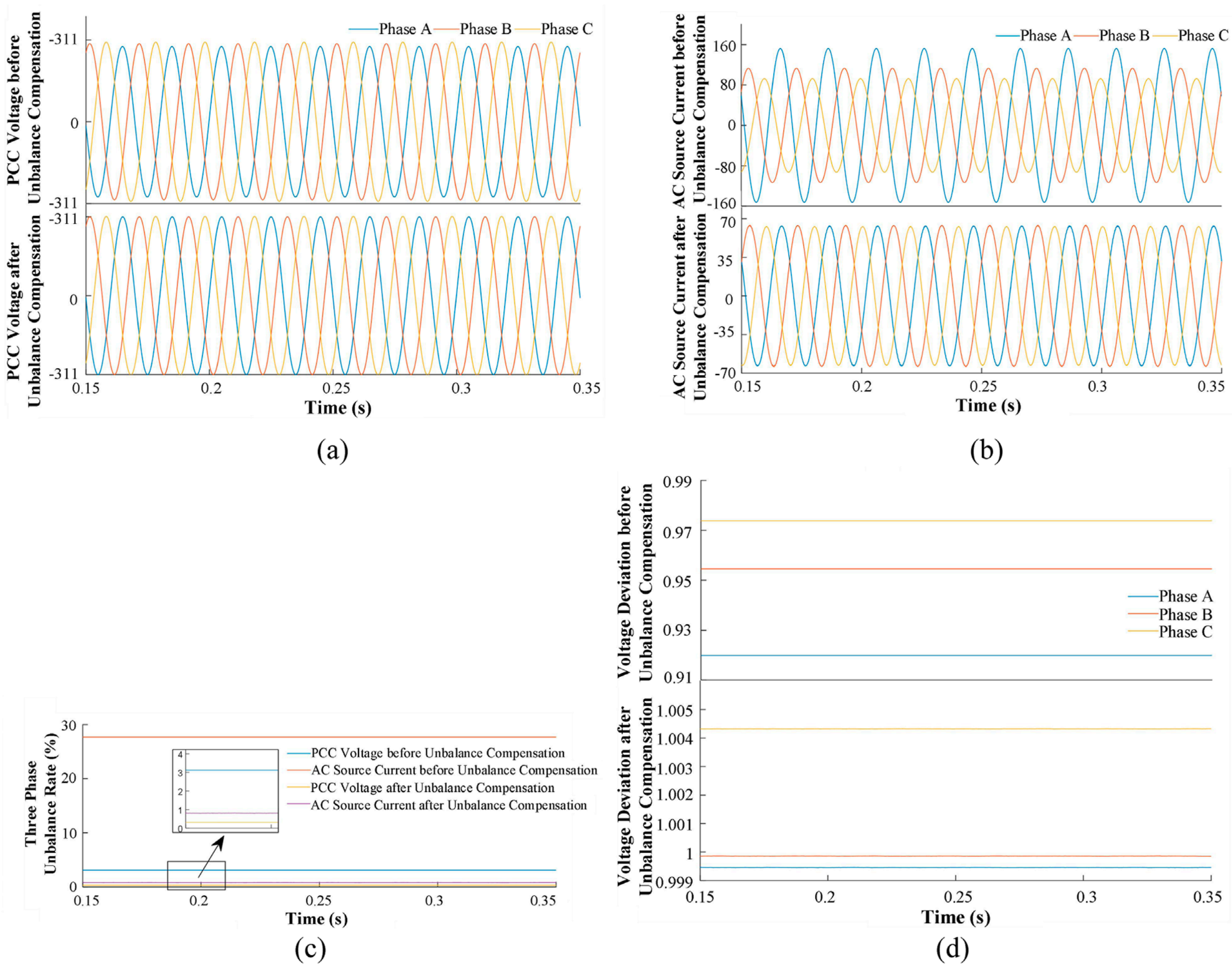

FIGURE 9
Comparison waveform under scenario 1 before and after the unbalance compensation. **(a)** PCC Voltage Waveform. **(b)** Grid-Side Output Current Waveform. **(c)**Three-Phase Unbalance Rate. **(d)** Voltage Deviation.

In Equation 16 u_α, u_β, i_α and i_β represent the $\alpha\beta$-axis voltage and current phasors at the PCC, constructed via SOGI, for single-phase voltage and current, respectively.

Due to the advantages of the Second-Order Generalized Integrator (SOGI), such as harmonic filtering, the SOGI (Wei et al., 2016) is adopted to construct the $\alpha\beta$-axis signals for u_{an}, u_{bn}, and u_{cn}, i.e., $u_{an\alpha}$, $u_{an\beta}$, $u_{bn\alpha}$, $u_{bn\beta}$, $u_{cn\alpha}$ and $u_{cn\beta}$. Therefore, based on the generalized instantaneous power theory for single-phase systems, the reference current commands for single-phase P/Q control are derived as

$$i_{kref} = 2 * \frac{u_{kn\alpha}p + u_{kn\beta}q}{u_{kn\alpha}^2 + u_{kn\beta}^2}(k = a, b, c) \tag{17}$$

4.2 PI-R control based double-frequency ripple suppression strategy for DC areas

The emergence of double-line-frequency voltage ripple components on the DC side, combined with the insufficient gain of conventional rectifier control loops at double-line-frequency, results in the inability of standard rectifier control systems to maintain stable DC voltage output under unbalanced load conditions. According to the Internal Model Principle, to achieve zero steady-state error tracking of the double-line-frequency pulsating components in the output voltage caused by load imbalance, the controller must incorporate sinusoidal internal models at the corresponding frequencies. This ensures that the open-loop magnitude-frequency characteristic curve of the system exhibits infinite gain at double-line-frequency (Zou et al., 2014; Ortega et al., 2021).

To address the double-line-frequency disturbances in the DC bus caused by three-phase imbalance in the AC distribution area, this paper employs a damped resonant controller to suppress the double-line-frequency pulsating components within the control loop. A voltage outer loop PI-R control strategy is proposed, with its expression given in Equation 17. The overall control block diagram of the VSC1 ripple suppression strategy is illustrated in Figure 5.

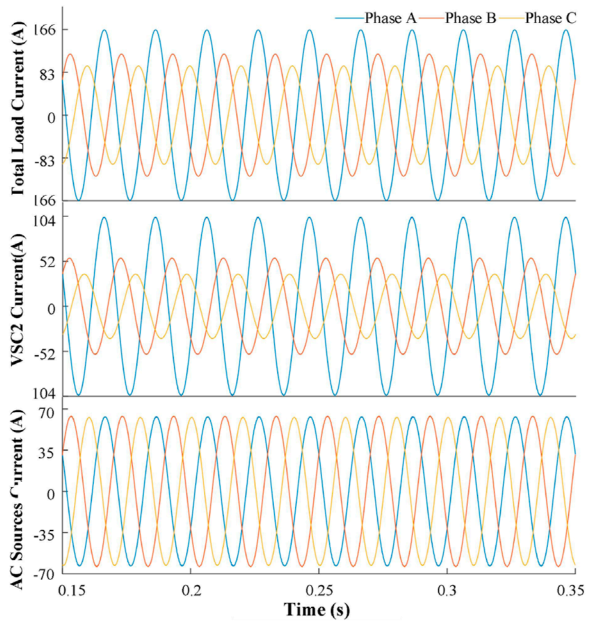

FIGURE 10
The current waveform on the load, AC sources and VSC2 sides under the compensation conditions.

$$G_{pir}(s) = k_p + \frac{k_i}{s} + \frac{2k_r\omega_c s}{s^2 + 2\omega_c s + \omega_0^2} \tag{18}$$

In Equation 18, k_p is the proportional coefficient, k_i is the integral coefficient, k_r is the gain coefficient, ω_c is the bandwidth coefficient, ω_0 is the resonant frequency.

Figure 6 shows the comparison of voltage loop frequency response characteristics between the conventional voltage outer loop and the inverter with the introduced resonant controller. The parameters of the PI-R controller are set as follows: proportional coefficient k_p = 1.787, integral coefficient k_i = 300, gain coefficient k_r = 150, bandwidth coefficient $\omega_c = \pi$, and resonant frequency is $2\pi^*2f$. From the Bode plot in Figure 6, it can be observed that after introducing the proposed resonant controller for double-frequency ripple suppression, the magnitude and phase frequency curves overlap with those of the traditional single-PI voltage outer loop in the low-frequency region. However, at twice the line frequency (100 Hz) of the inverter output, the PI + R control significantly increases the magnitude gain in the Bode plot, effectively enhancing the voltage loop's control over the double-frequency AC components in the output voltage caused by unbalanced loads. Additionally, the system achieves a cutoff frequency of 137 Hz and a phase margin of 34°, which satisfies the stability requirements.

5 Simulation verification and analysis

A simulation model of the dual-terminal low-voltage flexible interconnected grid, as shown in Figure 1, was developed on the MATLAB platform. The converter system parameters and control parameters are summarized in Tables 1, 2. Based on measurement data from a demonstration construction project in a city in Guizhou Province, this study analyzes whether the distribution area experiences operational issues such as three-phase imbalance and voltage deviation under typical conditions, with the power factor set to 0.9. The operational data for Distribution Area I are as follows:

Scenario 1: Data from 12:00 noon are selected as a typical case of high photovoltaic (PV) penetration and low load proportion, three phase load and photovoltaic access data for substation area I are summarized in Table 3.

Scenario 2: Data from 18:00 (6:00 p.m.) are selected as a typical case of high load proportion and low PV penetration. The three phase load and photovoltaic access data for substation area I are summarized in Table 4.

5.1 Verification of power quality optimization strategy for AC distribution areas

Scenario 1: Figures 7a–c illustrate the PCC voltage waveforms, source-side output current waveforms, and three-phase unbalance rates before and after implementing the proposed three-phase unbalance compensation control strategy. When the compensation strategy is blocked, the distribution area operated independently, with Distribution Area I bearing the full three-phase unbalanced load. The three-phase unbalance rate of its output currents entirely depended on the load level, resulting in a PCC voltage unbalance rate of approximately 3% and a source-side output current unbalance rate as high as 47%, exceeding the 2% three-phase unbalance limit. This severely compromised the stable operation of the distribution area. After enable the compensation strategy, the PCC voltage unbalance rate was reduced to nearly 0%, and the source-side current unbalance rate decreased to around 1.7%, significantly mitigating the three-phase imbalance and complying with the system's unbalance limit requirements.

Figure 7d shows the voltage deviation value before and after unbalance compensation. During the high PV penetration and low load proportion period (midday), the PV generation exceeded the load demand, causing reverse power flow and overvoltage at the PCC. As shown in Figure 7d, the voltage deviations without compensation for Phases A, B, and C were 1.084 pu, 1.08 pu, and 1.039 pu, respectively. The deviations for Phases A and B exceeded the upper limit of 1.07 pu, risking insulation damage to equipment. When the compensation strategy is enabled, Distribution Area I transferred a portion of PV generation to Distribution Area II, reducing its voltage deviation. The PCC phase voltage deviations stabilized around 1.013 pu, closer to the nominal value of 1 pu, thereby enhancing equipment safety.

Figure 8 shows the current waveforms at the source-side, load-side, and inverter-side under the compensation conditions. As demonstrated in Figure 8, after implementing the compensation control strategy, the inverter-side output current compensates for the unbalanced load-side output current, thereby reducing the three-phase unbalance rate of the source-side output current and mitigating its adverse impact on system stability.

Scenario 2: Figures 9a–c illustrate the PCC voltage waveforms, source-side output current waveforms, and three-phase unbalance rates before and after implementing the proposed three-phase unbalance compensation control strategy. As shown in Figures 9a–c,

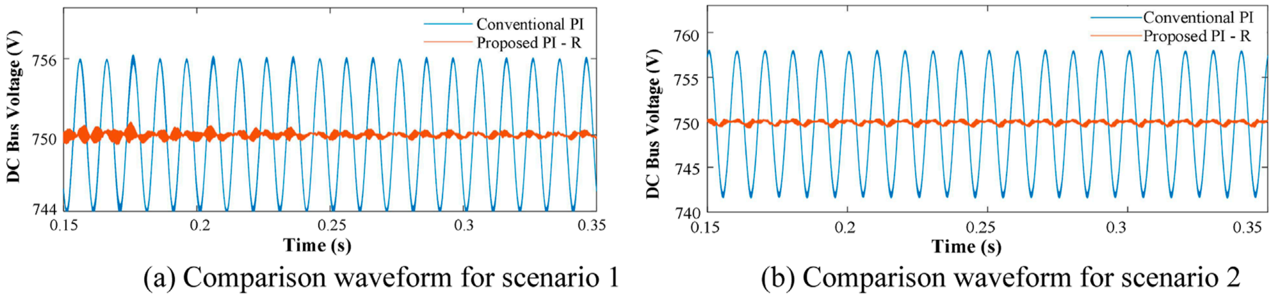

FIGURE 11
Comparison of PI and PI-R control voltage waveform under different scenarios. **(a)** Comparison waveform for scenario 1. **(b)** Comparison waveform for scenario 2.

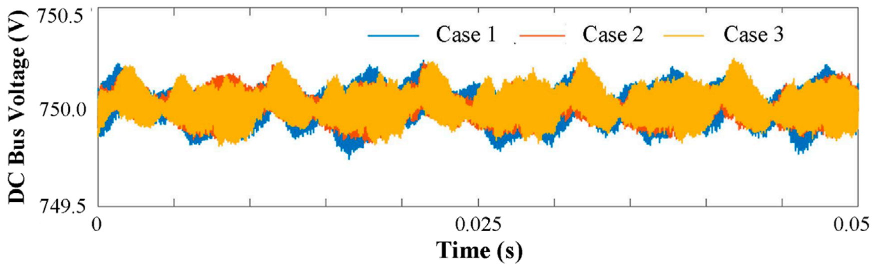

FIGURE 12
Suppression performance comparison of DC bus voltage ripple under different inductance parameters.

TABLE 5 The performance comparison for conventional and proposed strategy.

Scenario 1		Scenario 2	
Three-Phase Unbalance Rate	Before → After	Three-Phase Unbalance Rate	Before → After
PCC Voltage Unbalance Rate (%)	3%→0%	PCC Voltage Unbalance Rate (%)	3.1%→0.1%
Source-Side Output Current Unbalance Rate	47%→1.7%	Source-Side Output Current Unbalance Rate	27%→0.9%
Voltage Deviation Analysis	—	Voltage Deviation Analysis	—
Phase A	1.084→1.014	Phase A	0.92→0.9995
Phase B	1.08→1.013	Phase B	0.956→0.9998
Phase C	1.039→1.012	Phase C	0.974→1.0042
Double-Frequency Ripple Suppression Effect: Conventional PI Control: 12 V → PI-R Control: ~2 V		Double-Frequency Ripple Suppression Effect: Conventional PI Control: 14 V → PI-R Control: ~1 V	

under Scenario two operating conditions, the PCC voltage unbalance rate is approximately 3.1%, and the source-side output current unbalance rate reaches 27%, both exceeding the three-phase unbalance limit. After enable the compensation strategy, the PCC voltage unbalance rate is reduced to around 0.1%, and the source-side current unbalance rate decreases to 0.9%, effectively mitigating the three-phase imbalance and meeting the system's unbalance limit requirements. Figure 9d shows the voltage deviation waveforms before and after the unbalance compensation. During the low PV penetration and high load proportion period (evening), reduced PV generation combined with increased load demand leads to under voltage at the PCC. As seen in Figure 9d, the voltage deviations without compensation for Phases A, B, and C are 0.92 pu, 0.956 pu, and 0.974 pu, respectively. The deviations for Phases A and B fall below the lower voltage deviation limit (0.97 pu). When the compensation strategy is enabled, the PCC phase voltage deviations stabilize near 1 pu, ensuring safer operation of the distribution area. Figure 10 shows the current waveforms on the source side, the load side, and the inverter side under the compensation conditions. It can be seen that, after implementing the compensation control strategy, the output current on the inverter side compensates for the unbalanced output current on the load side, achieving three-phase balance on the source side.

5.2 Verification of the double-frequency ripple suppression strategy

Figure 11a, b show the double-line-frequency waveforms of the DC bus voltage under Scenarios one and 2, respectively, comparing traditional PI control with the PI-R control. As shown in Figures 11, 12, the conventional PI voltage outer loop fails to suppress the double-line-frequency pulsating components in the DC voltage. In contrast, the PI-R control effectively mitigates the double-frequency components by introducing a resonant controller into the traditional control loop, while maintaining excellent steady-state characteristics.

To validate the proposed strategy sensitive to the change of the inductance value,the suppression performance of DC bus voltage ripple under different inductance parameters are carried out. The results are plotted in Figure 12, in which three cases are set. All the inductance values both in inverter and rectifier side in Case 1 are reduced by 50%, and increase 50% in Case 3, and Case 2 keep the same value as Table 1. It can be seem that under different inductance variations, the double-frequency peak-to-peak ripple in dc bus voltage can be suppressed by the proposed method within the range of ±1 V, which fully demonstrates that the proposed strategy sensitive to the change of the inductance value.

Table 5 summarizes the performance comparison between the proposed control strategy and the traditional method under two scenarios. The results show that the proposed split-phase power decoupling method can reduce the power unbalance degree at the AC sources to less than 2%, which can ensure the safe and balanced operation of the AC transformer. Moreover, the proposed method can compensate for the voltage unbalance degree at the PCC point and simultaneously solve the voltage deviation problem. The proposed double-frequency ripple suppression method can effectively suppress the second - harmonic voltage, reducing the peak-peak DC voltage ripple pulsation to around 1–2 V at the minimum. The results fully demonstrate the effectiveness of the proposed control strategy.

6 Conclusion

This paper proposes a coordinated power quality improvement strategy for 3P4L-FCI based AC-DC distribution areas. To address issues such as three-phase imbalance and voltage limit violations in AC distribution areas, a split-phase power decoupling control strategy utilizing the three-phase four-leg converter is developed, effectively reducing the PCC voltage unbalance rate, source-side output current unbalance rate, and voltage deviations under two extreme operating conditions. Furthermore, by analyzing the double-line-frequency pulsation mechanism of the DC bus voltage under unbalanced AC distribution conditions, a double-frequency ripple suppression scheme based on a hybrid proportional-integral and resonant controller (PI-R) controller is proposed, which significantly mitigates the double-frequency components in the DC bus voltage. Finally, a MATLAB/Simulink-based simulation model of 3P4L-FCI based AC-DC distribution areas is established. The results validate the effectiveness of the proposed control strategies.

Data availability statement

The original contributions presented in the study are included in the article/supplementary material, further inquiries can be directed to the corresponding author.

Author contributions

QF: Conceptualization, Writing – original draft. JL: Conceptualization, Writing – review and editing. JZ: Conceptualization, Methodology, Writing – review and editing. YX: Funding acquisition, Supervision, Writing – review and editing. QH: Data curation, Investigation, Writing – review and editing. YG: Investigation, Validation, Writing – review and editing.

Funding

The author(s) declare that financial support was received for the research and/or publication of this article. This work was supported by Key Science and Technology Projects of China Southern Power Grid Corporation (GZKJXM20220041), and part by National Key Research and Development Program of China (2022YFE0205300).

Conflict of interest

Authors QF, JZ, YX, and YG were employed by Electric Power Research Institute of Guizhou Power Grid Co. Ltd. Authors JL and QH were employed by XJ Electric Co. Ltd.

The authors declare that this study received funding from China Southern Power Grid Corporation. The funder had the following involvement in the study: providing financial support for the construction of the simulation environment and data assistance, participated in manuscript revision and writing.

Generative AI statement

The authors declare that no Generative AI was used in the creation of this manuscript.

Publisher's note

References

Akagi, H., Watanabe, E. H., and Aredes, M. (2007). *Instantaneous power theory and applications to power conditioning*. Wiley-IEEE Press, 1–369. doi:10.1002/9781119307181

Bhowmick, S., Mukherjee, D., Basu, T. S., and Chakraborty, C. (2025). A three-phase four-leg neutral-point-clamped photovoltaic inverter with decoupled active and reactive power control and DC-link voltage ripple minimization under unbalanced grid operation. *IEEE Trans. Power Electron.* 40 (6), 7829–7843. doi:10.1109/tpel.2025.3538166

Cai, H., Guo, Q., Yang, R., et al. (2023). Dual-end grid-forming control of flexible DC transmission system for weak grid interconnection. *Electr. Power Autom. Equip.* 43 (09), 202–209. doi:10.16081/j.epae.202308014

Dong, H., Yuan, S., and Li, C. (2020). Power pulsation suppression of multi-source microgrid based on improved P/Q control. *J. Shenyang Univ. Technol.* 42 (01), 7–11. doi:10.79783/j.cnki.pspc.2217302

Fan, E., Zhao, L., and Li, Y. (2023). Second harmonic suppression and design of control parameters for a dual-active-bridge series resonant converter applied to a two-stage inverter. *Power Syst. Prot. Control* 51 (17), 58–68. doi:10.19783/j.cnki.pspc.221735

Gao, Y., Zhao, W., and Huang, S. (2016). Reactive power definitions in single-phase circuits based on instantaneous reactive power theory. *Electr. Meas. and Instrum.* 53 (20), 1–8. doi:10.3969/j.issn.1001-1390.2016.20.001

Huang, H., Chen, X., and Qu, Y. (2023). Distributed AC/DC converter and its active power decoupling control. *Power Electron.* 57 (10), 130–132+140. doi:10.3969/j.issn.1000-100X.2023.10.034

Liu, D., Liu, Z., Wang, T., Xie, Z., He, T., Dai, A., et al. (2023). A novel refined regulation method with modified genetic commutation algorithm to reduce three-phase imbalanced ratio in low-voltage distribution networks. *Energies* 16, 7838. doi:10.3390/en16237838

Lu, X., Sun, F., and Ma, W. (2020). Research on control strategy of three-phase four-leg inverter. *Electr. Meas. and Instrum.* 57 (12), 32–37. doi:10.19753/j.issn1001-1390.2020.12.006

Luo, X., Bian, D., and Zhao, X. (2023). Active power decoupling control strategy of single-phase inverter based on buck converter. *Water Resour. Power* 41 (06), 206–210. doi:10.20040/j.cnki.1000-7709.2023.20221534

Mocci, S., Ruggeri, S., and Pilo, F. (2025). Low-voltage renewable energy communities' impact on the distribution networks. *Energies* 18, 126. doi:10.3390/en18010126

Nguyen, M.-K., and Choi, Y.-O. (2018). PWM control scheme for quasi-switched-boost inverter to improve modulation index. *IEEE Trans. Power Electron.* 33 (05), 4037–4044. doi:10.1109/tpel.2017.2717487

Ortega, R., García, V. H., García-García, A. L., Rodriguez, J. J., Vásquez, V., and Sosa-Savedra, J. C. (2021). Modeling and application of controllers for a photovoltaic inverter for operation in a microgrid. *Sustainability* 13, 5115. doi:10.3390/su13095115

Shao, Y., and Ma, H. A. (2008). Triangle wave injection control strategy for three-phase four-leg inverter. *Electr. Meas. and Instrum.* (01), 48–51+60. doi:10.3969/j.issn.1001-1390.2014.19.015

Sheng, W., Liu, K., and Li, Z. (2024). Review of basic theory and methods of morphological evolution and safe and efficient operation of new distribution system. *High. Volt. Eng.* 50 (01), 1–18. doi:10.13336/j.1003-6520.hve.20232145

Shi, F., Ma, Y., and Xu, D. (2023). Improved stability control method of LCL-type grid-connected inverter under weak grid. *Renew. Energy Resour.* 41 (12), 1700–1704. doi:10.13941/j.cnki.21-1469/tk.2023.12.014

Si, J., Wu, X., Guo, Q., Hui, C., Liang, C., Junhui, H., et al. (2024). Review of flexible interconnection of regional grids interconnection planning and operation techniques for high percentage of renewable energy consumption. *Power Syst. Technol.*, 1–18. doi:10.13335/j.1000-3673.pst.2023.2116

Sun, Y., Chen, Y., and Shi, K. (2020). "Improved sequential control strategy for three-phase four-leg inverter." in Proceedings of the CSU-EPSA Shanghai, China. 32 (02), 105–112. doi:10.19635/j.cnki.csu-epsa.000183

Tan, C., Xing, Y., Chen, Q., and Liyan, Z. (2019). Anti-windup strategy of repetitive controller for three-phase four-leg grid-tied inverter. *Trans. China Electrotech. Soc.* 34 (17), 3631–3639. doi:10.19595/j.cnki.1000-6753.tces.180581

Tan, G., Guo, X., Zhao, W., Qi, L., and Sun, X. (2025). Second harmonic suppression for DC output voltage of three-phase four-leg PWM rectifier under unbalanced grid voltage conditions. *IEEE Trans. Power Electron.*, 1–17. doi:10.1109/tpel.2025.3551801

Tang, W., Zhang, Q., and Zhang, L. (2023). Concept, key technologies and development direction of multilevel AC/DC interconnection in new distribution system. *Automation Electr. Power Syst.* 47 (06), 2–17. doi:10.7500/AEPS20221031014

Tao, H., Yang, N., and Wang, H. (2023). Ripple analysis and control of MAPD cascaded H-bridge rectifier under capacitor mismatch. *Electr. Mach. Control* 27 (12), 145–158. doi:10.15938/j.emc.2023.12.015

Wang, L., Zang, S., and Li, C. (2024). A single-phase current-source converter based on the symmetrical half-bridge power decoupling topology. *Transactions of China Electrotechnical Society* 39 (24), 1–13. doi:10.19595/j.cnki.1000-6753.tces.231924

Wang, Z., Lin, J., and Chen, H. (2008). Control of distributed power inverter with unbalanced and nonlinear loads. *Automation Electr. Power Syst.* (01), 48–51+60. doi:10.3321/j.issn:1000-1026.2008.01.011

Wei, Z., Ru, X., and Shi, W. (2016). Control strategy for microgrid inverter under unbalanced load conditions. *Automation Electr. Power Syst.* 40 (20), 76–82. doi:10.7500/AEPS20151028004

Xiao, Q., Xu, J., and Jia, H. (2024). Analysis of the influence of overmodulation conditions on the operational stability of the hybrid modular multilevel. *J. Tianjin Univ. Sci. Technol.* 57 (02), 123–136. doi:10.11784/tdxbz202211030

Xu, Y., Liu, H., Xiong, X., Yu, J., Yao, S., Hai, Z., et al. (2022). Key technologies and development modes of flexible interconnection of low-voltage distribution station area. *Proceedings of the CSEE* 42 (11), 3986–4001. doi:10.13334/j.0258-8013.pcsee.210578

Xu, Y., Zhang, M., and Yang, Y. (2020). Dual quasi-proportional complex integral control strategy of the four-leg inverter with unbalanced load. *Power Syst. Prot. Control* 48 (07), 141–150. doi:10.19783/j.cnki.pspc.190490

Yan, F., Huang, L., and Wang, H. (2018). Composite control method for three-phase four-leg inverter. *J. Hebei Univ. Nat. Sci. Ed.* 38 (01), 105–112. doi:10.3969/j.issn.1000-1565.2018.01.016

Zeng, H., Xu, J., and Chen, D. (2018). Single-stage charging/discharging high-frequency link DC-AC converter with low-frequency harmonic suppression. *Trans. China Electrotech. Soc.* 33 (08), 1783–1792. doi:10.19595/j.cnki.1000-6753.tces.161912

Zhang, H., Cai, X., and Yang, X. (2017). Sequence decomposition control strategy for virtual synchronous generator based on three-phase four-leg inverter. *Power Syst. Technol.* 41 (04), 1291–1299. doi:10.13335/j.1000-3673.pst.2016.1790

Zhang, Y., Fu, W., and Liu, P. (2023). Research on four-switch power decoupling circuit based on AC-side of an inverter. *Electr. Mach. Control* 27 (08), 142–153. doi:10.15938/j.emc.2023.08.015

Zheng, G., Zhu, E., and Zhang, H. (2024). Flexible interconnection planning for distribution station areas of high-ratio photovoltaic based on master-slave game. *Electr. Power Constr.* 45 (04), 100–110. doi:10.12204/j.issn.1000-7229.2024.04.010

Zhou, J., and Lu, Z. (2025). Two-terminal three-phase unbalance management strategy for flexible interconnections taking into account DC doubling suppression. *Electric power automation equipment*. doi:10.16081/j.epae.202502008

Zou, C., Liu, B., Duan, S., and Li, R. (2014). Influence of delay on system stability and delay optimization of grid-connected inverters with LCL filter. *IEEE Trans. Industrial Inf.* 10 (03), 1775–1784. doi:10.1109/tii.2014.2324492